Magnetostriction reveals orthorhombic distortion in tetragonal Gd compounds

D. Betancourth,[1] V. F. Correa,[1] Jorge I. Facio,[1] J. Fernández,[1] V. Vildosola,[2] R. Lora-Serrano,[3,4] J. M. Cadogan,[4] A. A. Aligia,[1] Pablo S. Cornaglia,[1] and D. J. García[1]

[1]*Centro Atómico Bariloche and Instituto Balseiro, Comisión Nacional de Energía Atómica (CNEA), Consejo Nacional de Investigaciones Científicas y Técnicas (CONICET), Universidad Nacional de Cuyo (UNCUYO), Av. E. Bustillo 9500, R8402AGP San Carlos de Bariloche, Río Negro, Argentina*

[2]*Departamento de Materia Condensada, GIyA, CNEA, CONICET, (1650) San Martín, Provincia de Buenos Aires, Argentina*

[3]*Instituto de Física, Universidade Federal de Uberlândia, 38408-100, Uberlândia, MG, Brazil*

[4]*School of Physical, Environmental and Mathematical Sciences, UNSW Canberra at the Australian Defence Force Academy, Canberra, ACT, BC 2610, Australia*

(Received 29 May 2018; revised manuscript received 15 August 2018; published 2 April 2019)

We report detailed thermal expansion and magnetostriction experiments on $GdCoIn_5$ and $GdRh(In_{1-x}Cd_x)_5$ ($x = 0$ and 0.025) single-crystal samples that show a sudden change in the dilation at a field $B^\star$ for temperatures below the Néel transition temperature T_N. We present a first-principles model including crystal-field effects, dipolar and exchange interactions, and the dependence of the latter with lattice distortions in order to fully account for the magnetostriction and magnetic susceptibility data. The mean-field solution of the model shows that a transition between metastable states occurs at the field $B^\star$. It also indicates that two degenerate phases should coexist at temperatures below T_N, which may explain the lack of observation, in high-resolution x-ray experiments, of an orthorhombic distortion at the Néel transition, even though the experimentally determined magnetic structure breaks the tetragonal symmetry and the magnetoelastic coupling from our model is significant. These conclusions could be extended to other tetragonal Gd-based compounds that present the same phenomenology.

DOI: 10.1103/PhysRevB.99.134406

I. INTRODUCTION

Rare-earth magnetic compounds are among the strongest permanent magnets and present the highest magnetostrictive responses ever recorded. These remarkable properties stem from the large magnetic moments of the rare-earth ions with partially filled f shells and the magnetic anisotropy associated with crystal-field effects and spin-orbit couplings. The magnetic structure of these compounds is mainly determined by the Ruderman-Kittel-Kasuya-Yosida (RKKY) exchange interactions between the magnetic moments of the rare-earth ions and by the crystal field, which dominate over the dipolar interaction.

In many materials, magnetoelastic couplings lead to significant spontaneous lattice distortion concomitant with the magnetic order at zero applied magnetic field. In some systems, the associated changes in the lattice constants can be as large as a few percent [1]. When the symmetry of the magnetic order is lower than the lattice symmetry, a reduction of the latter is expected at the magnetic transition. This can occur, e.g., when the magnetoelastic couplings generate changes in the lattice parameters which do not preserve the lattice symmetry.

Among the rare-earth atoms, Gadolinium stands as different. In solid state compounds, it is generally found as a trivalent ion Gd^{3+} for which Hund's rules indicate the maximum spin allowed $\mathcal{S} = 7/2$, and zero angular momentum $\mathcal{L} = 0$. As a consequence of the latter, the magnetic coupling to the lattice via crystal-field effects is expected to be weak. The magnetic anisotropy observed in Gd compounds is therefore usually attributed to the dipolar interaction [2]. The dependence of the exchange couplings on the relative distance between ions can give rise to large magnetoelastic couplings.

Although a coupling between lattice and magnetic orders is observed on most Gd compounds there are few reports of lattice symmetry breaking at the magnetic transition (see Ref. [1] for a review).

Many Gd compounds with tetragonal lattice show antiferromagnetic (AFM) order [1,2]. Competing magnetic couplings can result in an AFM order other than the trivial G-AFM, where every pair of first neighbors is antiparallel. For instance, a second-neighbor AFM coupling can lead to a C-AFM order where chains of parallel-aligned moments order antiparallel (antiferromagnetically) between them along one of the [100] or [010] directions (see Fig. 1) [3,4]. If these chains are aligned along the basal plane, it is expected that below the AFM ordering temperature T_N, the lattice lowers its symmetry to orthorhombic [5]. Although symmetry-conserving distortions at the AFM transition have been detected [1], high-resolution x-ray difraction experiments do not show any difference between a and b lattice parameters [5,6]. Such an intriguing absence of lattice symmetry breaking at the Néel transition in Gd-based AFM systems has been referred to as the *magnetoelastic paradox* [5].

In this work, we present very sensitive dilation experiments across the Néel transition in $GdCoIn_5$ ($T_N \approx 30$ K) [7] and $GdRhIn_5$ ($T_N \approx 40$ K) [8]. Both systems show, for temperatures below T_N, an abrupt change of the longitudinal

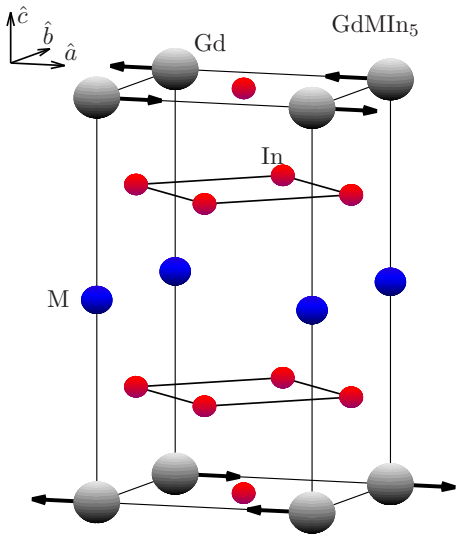

FIG. 1. Crystal structure of the 115 compounds. The observed magnetic configuration (C-AFM) is indicated by the thick arrows on the Gd atoms. The spins are parallel to the $\hat{a}$ axis.

linear forced magnetostriction in an external field of ∼1 T. We perform detailed calculations which indicate that the dipolar interaction [2], the crystal electric field (CF) [9], and the strain dependence of the magnetic exchange couplings are all necessary to account for the observed lattice distortions and magnetic structure. The importance of CF effects on Gd compounds has been discussed on Ref. [9] for the specific case of $GdRhIn_5$, and for other compounds on Refs. [10,11]. Anisotropic RKKY exchange couplings (where for instance out-of-plane components of the magnetic moments couple differently to the in-plane components) could also be present via 5*d* Gd electrons [12,13]. To keep the complexity of the problem at a reasonable level we choose not to consider this last possibility and keep only isotropic couplings between different neighbours (as calculated on Ref. [14]) . We also show that the dilation data are compatible with the existence of a tetragonal to orthorhombic distortion of the lattice at the Néel transition. The predicted orthorhombic distortions result from the competition between the different magnetoelastic couplings.

A so-called "2q" structure has been proposed in Refs. [15,16], to explain the magnetoelastic properties of $GdNi_2B_2C$ and the magnetoelastic paradox. The model used in Ref. [16] leads however to an infinitely degenerate ground state if no lattice distortions are allowed. Our extended model that includes crystal field effects, lifts this degeneracy and leads to the experimentally observed single-q configuration for $GdRhIn_5$. Despite of using the best achievable resolution from single-crystal XRD data, E. Granado *et al.* [6] did not find the proposed structure symmetry reduction nor any anomaly in the evolution of the full width at half maximum (FWHM) with temperature of *hh*0 or *h*00 diffraction lines on $GdRhIn_5$. Our current results therefore suggest that the structural distortion observed in $GdRhIn_5$ is taking place within the experimental XRD uncertainty. This makes the experimental detection largely sample dependent; i.e., slightly different single-crystal surface domain structures would hinder the observation.

The rest of this paper is organized as follows. Section II presents the main experimental and theoretical results for the magnetostriction and thermal expansion data for the $GdCoIn_5$ and $GdRhIn_5$ compounds. Section III presents the model, while Sec. IV presents the numerical simulations and their interpretation. Finally, in Sec. V, we present the conclusions.

II. EXPERIMENT

We present below the main experimental and theoretical results on the magnetostriction and thermal expansion data for the $GdCoIn_5$ and $GdRhIn_5$ compounds. Both materials crystallize in the tetragonal $HoCoGa_5$ structure (see Fig. 1). The magnetic structure inferred by x-ray magnetic scattering experiments in $GdRhIn_5$ is of C-type [6] (see Fig. 1).

The high-quality single crystals used in the present work were grown by the self-flux technique. Samples of $GdCoIn_5$ (GCI) and $GdRhIn_5$ (GRI) come from batches grown in Bariloche (Argentina) [7,17], while $GdRh(In_{0.975}Cd_{0.025})_5$ samples come from Uberlandia (Brazil). The starting materials were mixed in the nominal ratio Gd : Rh : In : Cd = 1 : 1 : 20-x : x, as for Cd-doped $CeRhIn_5$ [18]. The grown single crystals were confirmed by powder x-ray diffraction to crystallize also in the $HoCoGa_5$-type structure with no traces of secondary phases. The specific heat and the magnetic susceptibility data are compatible with $S = 7/2$ spins at the Gd^{3+} ions coupled by exchange interactions mediated by the conduction electrons. The main difference between $GdCoIn_5$ and $GdRhIn_5$ is the larger exchange coupling along the c axis in the latter which leads to a higher T_N [14].

Platelet-shaped crystals of typical size 1 × 1 × 0.4 mm^3 were selected for the dilation experiments which were performed with a high-resolution ($\Delta L \leqslant 1$ Å) capacitive dilatometer [19]. All dilation experiments under magnetic field were carried out in the longitudinal configuration, i.e., with the magnetic field B parallel to the sample dimension L being measured.

Figure 2 summarizes the most important experimental observations from this work. It displays the forced magnetostriction (lattice dimension change driven by an external magnetic field) along the $\hat{a}$ axis for both GCI and GRI. At temperatures below T_N, $\Delta L_a/L_a$ shows a sudden increase at an in-plane field $B^\star \sim 1$ T. Above this field, $\Delta L_a/L_a$ becomes field independent for GCI and shows a weak increase with increasing magnetic field for GRI. This weak upturn may arise from a small contribution from the c axis, since it is not observed in GRI single crystals from a different source nor in Cd doped crystals. Other than this, there is full quantitative and qualitative agreement (values of $B^\star$ and $\Delta L_a/L_a$ for instance) between samples from different sources and batches [see the $\hat{a}$-axis magnetostriction for $GdRh(In_{0.975}Cd_{0.025})_5$ in the same figure]. No hysteresis effects are observed. At temperatures above T_N the magnetostriction becomes negligible and no sudden change is observed. This type of change in ΔL for $T < T_N$ is usually seen on ferromagnetic materials and attributed to the change from the zero magnetization to the saturated magnetic state (see Chap. 1 on Ref. [20]). As we will see in the following section, in these antiferromagnetic systems an

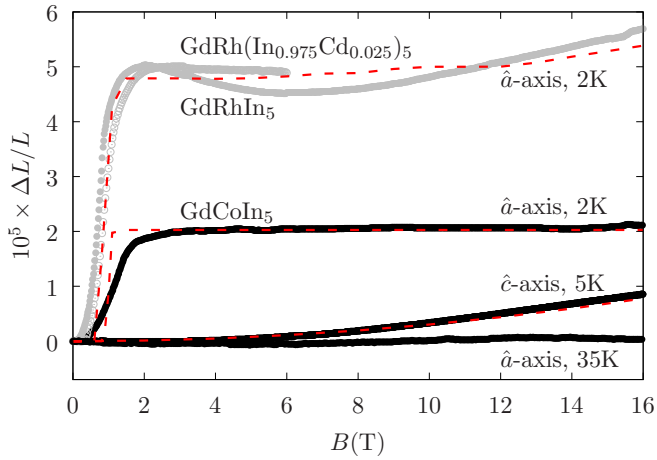

FIG. 2. Solid symbols: experimental forced magnetostriction for $GdCoIn_5$ (black symbols) and $GdRhIn_5$, $GdRh(In_{0.975}Cd_{0.025})_5$ (grey symbols with filled and empty circles, respectively) at different temperatures and along different directions as indicated in the figure. Dashed lines: calculated forced magnetostriction (see main text).

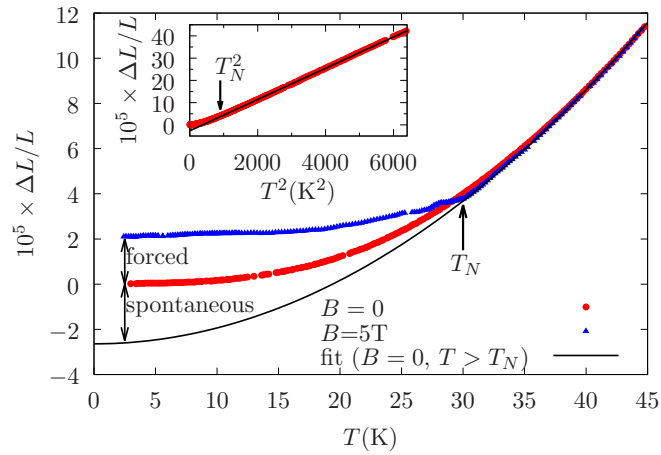

FIG. 3. Thermal expansion along the $\hat{a}$ axis as a function of the temperature for $GdCoIn_5$ at $B = 0$ and 5 T. The spontaneous and forced magnetostrictions are indicated in the figure. The nonmagnetic contribution (thin line) is obtained from a linear fit of the thermal expansion versus T^2 at $B = 0$ and for $T > T_N$ as shown in the inset.

applied magnetic field induces a spin-flop transition (at the field $B^\star$) to a metastable state where the spins point mainly along the $\hat{c}$ axis [21,22]. To account for the value $B^\star$ and the absence of hysteresis both the dipole interaction and the effect of the crystal field in second order perturbation theory needs to be considered in the calculations. The theoretical results (dashed lines in Fig. 2), were obtained using fitting interaction parameters constrained to the range of estimated values (see Sec. III).

Along the $\hat{c}$ axis, the field dependence of the forced magnetostriction (MS) is quadratic at all temperatures as it is shown in Fig. 2 for GCI. GRI mimics this behavior (not shown here).

The spontaneous and the forced magnetostrictions are a measure of the strength of the magnetoelastic couplings which can be extracted from the thermal expansion data. The main panel of Fig. 3 shows the $\hat{a}$-axis thermal expansion $\Delta L_a/L_a$ of GCI at zero field and at $B = 5$ T $> B^*$. A small kink signposts the magnetic transition at T_N. In the paramagnetic state ($T > T_N$), $\Delta L_a/L_a$ is proportional to T^2 in a very good approximation, as seen in the inset of Fig. 3. This quadratic nonmagnetic thermal-expansion background (which implies a nearly constant thermal expansion coefficient divided by T, as reported in Ref. [7]) is also included in the main panel and it extrapolates at low temperatures to ΔL_a (nonmagnetic, $T \to 0)/L_a = -2.5 \times 10^{-5}$. We take the quadratic fit as the nonmagnetic thermal expansion, and the difference between the zero-field thermal expansion curve and that fit corresponds to the spontaneous MS. Accordingly, the difference between the finite field and the zero-field data is the forced MS. The total MS is the sum of the forced and the spontaneous MSs and can be obtained subtracting to the finite field curve the nonmagnetic fit.

According to this analysis, the $\hat{a}$-axis spontaneous MS is positive in GCI, resulting in a zero temperature expansion $\Delta L_a(B = 0, T \to 0)/L_a - \Delta L_a$ (nonmagnetic, $T \to 0)/L_a = 2.5 \times 10^{-5}$, while the forced MS is also positive giving $\Delta L_a(B = 5\ \text{T}, T \to 0)/L_a - \Delta L_a(B = 0, T \to 0)/L_a = 2 \times 10^{-5}$. The zero-temperature spontaneous and forced MS of both GCI and GRI are summarized in Table I. An equivalent analysis can be performed from the thermal expansion data along the $\hat{c}$ axis. In this case, however, the spontaneous MS has the opposite sign $\Delta L_c(T \to 0)/L_c = -1.2 \times 10^{-5}$.

The theoretical description of the MS data needs also to account for the pronounced anisotropy observed in the magnetic susceptibilities below T_N as it was reported previously [8,23]. Interestingly, the observed difference between the $\hat{a}$-axis and $\hat{c}$-axis susceptibilities is rapidly suppressed as the magnetic field is raised above ∼1 T [23,24].

III. THEORY

In this section, we present the model used to describe the experimental data. We present the different magnetic interaction terms in the Hamiltonian and analyze their coupling to the lattice degrees of freedom.

A. Exchange interactions

The magnetic exchange interactions between localized magnetic moments at the Gd^{3+} ions were determined by magnetic susceptibility and specific heat experiments combined with first-principles calculations [7,14]. Density functional theory (DFT) was used to compute the energy of different magnetic configurations as detailed in Ref. [14]. From those

TABLE I. Measured and calculated spontaneous and forced magnetic expansions $\Delta L/L$ for $\hat{a}$-axis and $\hat{c}$-axis measurements.

$10^5 \times \Delta L/L$	$GdCoIn_5$ ($\hat{a}$)	$GdRhIn_5$ ($\hat{a}$)	$GdCoIn_5$ ($\hat{c}$)
Spontaneous (exp.)	2.5	3.4	−1.2
Spontaneous (calc.)	2.0	2.6	−4.7
Forced (exp.)	2.0	4.9	0.9
Forced (calc.)	2.0	4.9	0.9

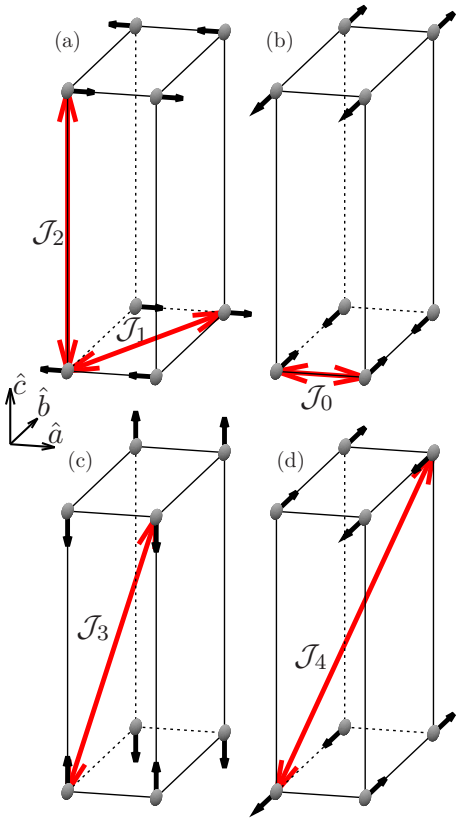

FIG. 4. Different magnetic arrangements and main exchange couplings. The small single headed arrows indicate the magnetic moment of the Gd^{3+} ions, the double headed arrows indicate the exchange couplings $\mathcal{J}_i$ between the magnetic moments. (a) Ferromagnetic chains along the $\hat{a}$ axis with the spins parallel to the same axis (C-AFM$_{aa}$). (b) Ferromagnetic chains along the $\hat{a}$ axis with the spins parallel to the $\hat{b}$ axis (C-AFM$_{ab}$) and $\hat{c}$ axis (c) C-AFM$_{ac}$. (d) Analogous to (a) with the chains and the spins along the $\hat{b}$ axis (C-AFM$_{bb}$).

energies exchange couplings between Gd^{3+} ions were determined. Quantum Monte Carlo calculation of the magnetic susceptibility and specific heat using those couplings agree with the corresponding experimental results on $GdRhIn_5$ and $GdCoIn_5$ [7,14]. The exchange interactions up to the fifth nearest neighbor are presented in Fig. 4. These couplings do not determine unambiguously the magnetic ground state as the energy only depends on the relative orientation of the magnetic moments. Figure 4 presents four different magnetic moment arrangements having the same exchange energy.

The exchange couplings $\mathcal{J}_i$, shown on Fig. 4, are modified when the lattice is distorted

$$\mathcal{J}_i(\delta a, \delta b, \delta c) \simeq \mathcal{J}_i + \frac{d\mathcal{J}_i}{da}\delta a + \frac{d\mathcal{J}_i}{db}\delta b + \frac{d\mathcal{J}_i}{dc}\delta c, \quad (1)$$

where δa, δb, and δc are uniform lattice distortions along the $\hat{a}$, $\hat{b}$, and $\hat{c}$ axes, respectively. The magnetic exchange interaction between magnetic moments $\vec{S}_i$ at the Gd^{3+} ions can be written as

$$H_E = \sum_{\langle i,j\rangle} \mathcal{J}_{i,j}(\delta a, \delta b, \delta c)\, \vec{S}_i \cdot \vec{S}_j, \quad (2)$$

where the $\mathcal{J}_{i,j}$ couplings are equal to $\mathcal{J}_0$ for first nearest neighbors, $\mathcal{J}_1$ for second nearest neighbors, etc.

Although this interaction and its dependence with the lattice distortions is the largest, it is not enough to explain the observed ground-state configuration, nor the magnetoelastic data or the magnetic anisotropy. For example, the Hamiltonian given by Eq. (2) leads to the same energy for the C-AFM$_{aa}$ and the C-AFM$_{ac}$ configurations. As we show below, the dipolar interactions break this degeneracy.

B. Dipolar interactions

The dipolar interactions have an explicit dependence with the distance between spins:

$$H_D = 16.8\ \text{K} \sum_{i,j} \frac{a_B^3}{r_{ij}^3}\left(\vec{S}_i \cdot \vec{S}_j - \frac{3}{r_{ij}^2}(\vec{S}_i \cdot \vec{r}_i)(\vec{S}_j \cdot \vec{r}_j)\right), \quad (3)$$

where K is Kelvin scale unit, a_B is the Bohr radius, r_i is the position of the ith spin and $r_{ij} = |\vec{r}_i - \vec{r}_j|$.[1] Note that here and in what follows we take $k_B = 1$ and use K for the energy units. H_D introduces a magnetic anisotropy. Since the distance between nearest-neighbor spins is larger along the $\hat{c}$ axis than along the $\hat{a}$ or $\hat{b}$ axis, the dipolar configurations with the lowest energy have the spins in the a-b plane. Still those states remain highly degenerate as a continuum of configurations with in-plane second nearest neighbors antiparallel have the same exchange and dipolar energies [see e.g., in Figs. 4(a), 4(d), and 6]. The experimentally observed order are however the ones shown in Figs. 4(a) and 4(d). The first state, Fig. 4(a), becomes the lowest lying state under a distortion $a \to a + \delta a$ and $b \to b + \delta b$ such that the lattice parameters a and b become different (orthorhombic distortion).

The uniaxial magnetic anisotropy along the $\hat{c}$ axis introduced by the dipolar interaction is however larger than what is inferred from the value of $B^\star$ (see Appendix A). An additional source of magnetic anisotropy, which is due to crystal-field effects, needs to be considered to explain the value of $B^\star$.

C. Crystal-field effects

The Gd^{3+} ion is, according to Hund's rules, in a $4f^7$ state with $\mathcal{L} = 0$. The spin-orbit $\sum_i \vec{\sigma}_i.\vec{l}_i$ coupling, however, mixes this $\mathcal{L} = 0$, $S = 7/2$ state with a higher energy multiplet with $\mathcal{L} = 1$, $S = 5/2$, and $J = 7/2$ (see Appendix B for details), which is affected by the tetragonal crystal field. As a consequence crystal field (CF) effects, although small, are present and need to be considered.

The total crystal-field effect can be written as

$$H_{CF} = \sum_i B_2 S_{ic}^2 + A(\delta a - \delta b)\left[S_{ia}^2 - S_{ib}^2\right], \quad (4)$$

where $S_{i\ell}$ is the component of the ith spin along the $\hat{\ell}$ axis. The first term in Eq. (4) is the intrinsic CF [10] and the last term is induced by distortions between the a and b lattice parameters (see Ref. [25]). The contribution due to c deformations is

[1]The value of 16.8 K comes from the universal constants combination $\frac{g^2\mu_0\mu_B^2}{4\pi a_B^3}$, where $g = 2$ is the gyromagnetic factor for Gd^{3+}.

TABLE II. Coupling parameters. $\frac{d\mathcal{J}_0^a}{da}$ corresponds to the rate of change of $\mathcal{J}_0$ due to a lattice distortion parallel to the coupling while $\frac{d\mathcal{J}_0^a}{db}$ corresponds to a distortion in the perpendicular direction on the a-b plane.

Parameter	$GdCoIn_5$	$GdRhIn_5$
$\mathcal{J}_0$	1.31 K	1.21 K
$\mathcal{J}_1$	1.65 K	1.74 K
$\mathcal{J}_2$	0.47 K	1.43 K
$\mathcal{J}_3$	0.05 K	− 0.10 K
$\mathcal{J}_4$	− 0.11 K	− 0.15 K
$\frac{d\mathcal{J}_0^a}{da}$	0.61 K/Å	− 2.4 K/Å
$\frac{d\mathcal{J}_0^a}{db}$	− 1.39 K/Å	− 2.9 K/Å
$\frac{d\mathcal{J}_1}{da}$	0.265 K/Å	0.066 K/Å
A	0.49 K/Å	1.26 K/Å
B_2	− 0.058 K	− 0.019 K
$\frac{d\mathcal{J}_1}{dc}$	− 1.0 K/Å	–

negligible with respect to the intrinsic contribution $B_2 S_c^2$. The negative sign of B_2 is expected as the compound $TbRhIn_5$ has a strong c-axis anisotropy, mostly dominated by a B_2 term (see Ref. [26]). We also estimate the magnitude of this coefficient as the crystal field present on $TbRhIn_5$ can be translated to $GdRhIn_5$ (see an example of this procedure in Ref. [27]). Using that procedure the resulting intrinsic crystal field for Gd^{3+} on $GdRhIn_5$ is mainly given by the second order term with $B_2 \sim -8.4$ mK. The precise value for $GdRhIn_5$ and $GdCoIn_5$ (see Table II) was obtained fitting the experimental magnetostriction results (its main effect is to determine $B^\star$ when combined with the dipolar contribution).

D. Elastic energy

The elastic energy for a uniform distortion can be approximated as

$$H_{el} = \tfrac{1}{2} C_{el}^{ab} (\delta a^2 + \delta b^2) + \tfrac{1}{2} C_{el}^{c} \delta c^2 \tag{5}$$

where the elastic constants $C_{el}^{ab} \sim C_{el}^{c} \sim C_{el} = 70\,000$ K/Å^2 are estimated from the elastic properties of materials of the same family of compounds [28,29] and density functional theory (DFT) results (see Appendix C).

IV. NUMERICAL SIMULATIONS

The total Hamiltonian of the system is obtained combining Eqs. (2)–(5):

$$H = H_{el} + H_D + H_E + H_{CF}. \tag{6}$$

To evaluate this energy, we approximate the large $S = 7/2$ spins on the Gd^{3+} ions with classical magnetic moments (for our case with $J_1/J_0 > 1$, we do not expect this approximation to change the ground-state correlations, see Ref. [30] for a related system). We consider a lattice of $L \times L \times L$ sites. We find that $L \gtrsim 12$ is enough to obtain L-independent results.

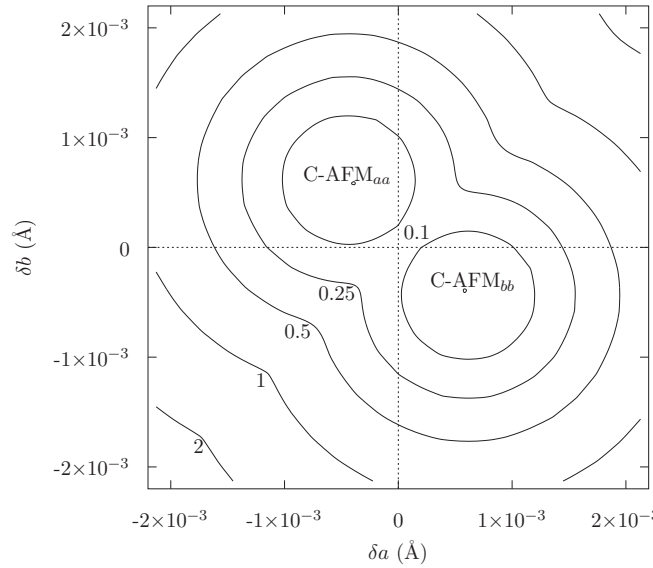

FIG. 5. Total energy (in degrees Kelvin) relative to the C-AFM$_{aa}$ configuration energy (E_{aa}) as a function of the changes in the lattice parameters δa and δb.

We minimize the energy considering uniform deformations δa, δb, δc, and spin rotations restricted to magnetic orders that preserve the eight-site magnetic unit cell of Fig. 4.

The coupling parameters used in the simulations of $GdCoIn_5$ and $GdRhIn_5$ are presented in Table II. The exchange coupling parameters were obtained from DFT calculations [14]. The remaining parameters were obtained fitting the magnetostriction and the magnetic susceptibility. Reference values for the rate of change of the exchange coupling with the lattice parameter changes were obtained from DFT calculations (for details see Ref. [31])

A. Ground state for zero magnetic field ($B = 0$)

The total energy as function of δa and δb is shown on Fig. 5. Two degenerate minima are obtained with magnetic orders C-AFM$_{aa}$ (see Fig. 4) and C-AFM$_{bb}$, which is related to C-AFM$_{aa}$ by a rotation of the lattice by 90° around the $\hat{c}$ axis. In the C-AFM$_{bb}$ configuration the spins and the spin chains are along the $\hat{b}$ axis. The distortions associated with these minima satisfy $\delta a_{aa} \neq \delta b_{aa}$ and $\delta a_{aa} = \delta b_{bb}$, $\delta b_{aa} = \delta a_{bb}$. The fact that in our simulations $\delta a_{aa} \neq \delta b_{aa}$ indicates that the ground-state crystal symmetry is reduced from tetragonal to orthorhombic.

From here on we model the real system by assuming that it is composed by a mixture of these two states and consider the average of both distortions [6,16]

$$\bar{\delta a} = (\delta a_{aa} + \delta a_{bb})/2, \tag{7}$$

$$\bar{\delta b} = (\delta b_{aa} + \delta b_{bb})/2 \tag{8}$$

to compare with the experimental results. The situation should be quite similar to $YBaCu_3O_{6+x}$ and a large amount of domain states should spread throughout the crystal to minimize the elastic energy [32,33]. Assuming a homogeneous distortion of the lattice, we have $\Delta L_a/L_a = \bar{\delta a}/a$. In the zero-field case

TABLE III. Calculated distortions δa, δb for the $B = 0$ and 2 T (field parallel to the $\hat{a}$ axis) cases. The Lattice parameter a is 4.568(3)Å for $GdCoIn_5$ and 4.651(8)Å for $GdRhIn_5$ (see Ref. [6]).

	B	$GdCoIn_5$	$GdRhIn_5$
δa_{aa}	0	-4.4×10^{-4} Å	-4.8×10^{-4} Å
δa_{bb}	0	6.2×10^{-4} Å	7.2×10^{-4} Å
δb_{aa}	0	6.2×10^{-4} Å	7.2×10^{-4} Å
δb_{bb}	0	-4.4×10^{-4} Å	-4.8×10^{-4} Å
$10^5\times\Delta L/L$	0	2.0	2.6
δa_{ac}	2 T	-2.5×10^{-4} Å	-0.2×10^{-4} Å
δa_{bb}	2 T	6.2×10^{-4} Å	7.2×10^{-4} Å
δb_{ac}	2 T	4.4×10^{-4} Å	1.3×10^{-4} Å
δb_{bb}	2 T	-4.4×10^{-4} Å	-4.8×10^{-4} Å
$10^5\times\Delta L/L$	2 T	4.0	7.5

($B = 0$), we have $\delta\bar{a}/a \equiv \delta\bar{b}/b$, which corresponds to the spontaneous MS, since the model does not consider nonmagnetic distortions. These distortions are presented in Table III and show a good agreement with the experimental results (see Table I). The magnitude of this orthorhombic distortion for $GdRhIn_5$ ($\frac{|b-a|}{a} = 2.6\times10^{-4}$), is comparable to the estimated upper limit obtained from XRD experiments[$\frac{|b-a|}{a} = 2\times10^{-4}$] [6].

B. Magnetostriction

To analyze the effect of an external magnetic field on the striction, we include the Zeeman coupling

$$H_Z = \sum_i -g\mu_B \vec{S}_i \cdot \vec{B}. \tag{9}$$

Under a magnetic field along the $\hat{a}$ axis, the energy of the C-AFM$_{aa}$ spin configuration remains unchanged while the energy of the C-AFM$_{bb}$ configuration [see Fig. 4(d)] is reduced. A large energy barrier separates however these two configurations. To change from C-AFM$_{aa}$ to C-AFM$_{bb}$ at zero field, the distortions need to be interchanged $\delta a \leftrightarrow \delta b$, the spins rotated 90° interchanging nearest-neighbor correlations from antiferromagnetic along the $\hat{a}$ axis to ferromagnetic, and vice versa along the $\hat{b}$ axis. Although the C-AFM$_{ac}$ order has a larger energy than C-AFM$_{bb}$, it is much closer in configuration space to C-AFM$_{aa}$. The spin-spin correlations do not change and the distortions are only slightly modified as they are determined to a large extent by these correlations. The exchange coupling only depends on the relative orientation of the spins. Our numerical results show that for a field $B > B^\star$ the configuration CAFM$_{ac}$ has a lower energy than CAFM$_{aa}$ and a transition between these two metaestable phases should occur. The critical field $B^\star$ is determined by the dipolar energy and the intrinsic crystal field parametrized by B_2. For these compounds the CF reduces the critical field as it lowers the energy of the CAFM$_{ac}$ configuration. At $B = B^\star$ an energy barrier separates the C-AFM$_{bb}$ and the C-AFM$_{ac}$ configurations.

In our scenario, the regions of the sample which at zero field were in the C-AFM$_{aa}$ configuration, with distortions $\delta a_{aa}, \delta b_{aa}$ have, at $B = B^\star$, a sudden change

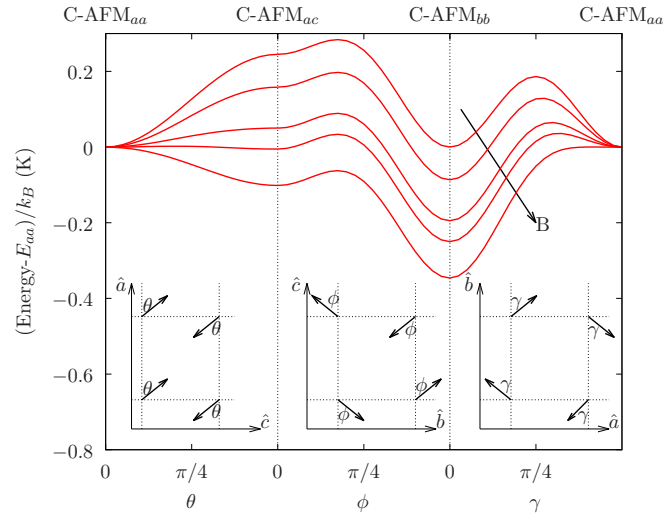

FIG. 6. Total energy of the system relative to the C-AFM$_{aa}$ configuration energy for a path in configuration space joining the C-AFM$_{aa}$, C-AFM$_{ac}$, and C-AFM$_{bb}$ phases. The spins are tilted uniformly by an angle as indicated in the figure. Different lines correspond to different values of the external magnetic field parallel to the $\hat{a}$ axis ($B = 0$, 0.5, 0.75, 0.85, and 1 T).

to the C-AFM$_{ac}$ spin configuration with different distortions δa_{ac} and δb_{ac} (see Table III). The regions of the sample in the C-AFM$_{bb}$ configuration, however, remain in it and the field only tilts the spins slightly in its direction. This leads to a forced MS at a field $B > B^\star$ given by $\Delta L_a(B, T = 0)/L_a - \Delta L_a(B = 0, T = 0)/L_a = [\delta a_{ac}(B) + \delta a_{bb}(B) - \delta a_{aa}(B = 0) + \delta a_{bb}(B = 0)]/(2L_a)$, which is presented in Table I for $GdCoIn_5$ and $GdRhIn_5$ at $B = 5$ T.

For low fields, $B < B^\star$, only the deformations associated with the C-AFM$_{bb}$ order change. This is reflected on a small change of the total deformation. Around the critical field, there is a sudden change of the deformations following the change of the magnetic order from C-AFM$_{aa}$ to CAFM$_{ac}$.

Figure 6 presents the energy of the system for a path in the space of spin configurations that passes through the C-AFM$_{aa}$, C-AFM$_{ac}$, and C-AFM$_{bb}$ phases. To go from one configuration to the other, each spin is rotated by the same angle and the energy is minimized with respect to distortions δa, δb, and δc. In the absence of an external field, there are two degenerate minima for the C-AFM$_{aa}$ and C-AFM$_{bb}$ configurations. While the energy E_{aa} of the C-AFM$_{aa}$ configuration does not depend on the magnetic field, both the C-AFM$_{ac}$ and C-AFM$_{bb}$ lower their energy with increasing magnetic field. At a field $B^\star \sim 0.85$ T the C-AFM$_{aa}$ configuration becomes unstable and there is a transition to the C-AFM$_{ac}$ phase. This transition has a very small hysteresis loop of width ∼0.01 T, which is not observed in the experiments. Even for fields $B \sim 16$ T a barrier separates the C-AFM$_{ac}$ and C-AFM$_{bb}$ phases. We present in Appendix A, a minimal model that captures the main physical ingredients and allows to obtain the model parameters from the experimental results.

The magnetostriction with the magnetic field parallel to the $\hat{c}$ axis is simpler to understand because, in this case, there is no spin-flop transition. As the magnetic field is increased, the

local spins tilt in the $\hat{c}$ direction. This leads to a change in the spin-spin correlations of antiparallel spins

$$\delta\langle\vec{S}_i \cdot \vec{S}_j\rangle \sim -\frac{S^2}{2}\left(\frac{M(B)}{M_S}\right)^2, \tag{10}$$

where $M(B) \ll M_S$ is the uniform magnetization along the $\hat{c}$ axis and M_S is its saturation value. Since $M(B) \propto B$, this results, to leading order, in a c lattice parameter change $\delta c \propto B^2$.

V. SUMMARY AND CONCLUSIONS

We analyzed the magnetoelastic properties of $GdCoIn_5$ and $GdRhIn_5$. We measured the thermal expansion and the longitudinal magnetostriction on single crystals using a high-resolution capacitive dilatometer. The observed data have been accounted from a first-principle model.

These compounds present a number of intriguing properties. The observed magnetic order below T_N is a C-type antiferromagnet which has a lower point symmetry than the lattice, but the expected tetragonal to orthorhombic distortion is not observed with high-resolution XRD experiments in zero applied field. The in-plane dilation presents a sudden change at a field $B^\star \sim 1$ T and temperatures below the Néel transition which is not observed along the $\hat{c}$ axis (for fields along the same axis). A similar behavior is seen in sligthly Cd-doped samples. Contrary to expectations for a spin-flop transition [34,35], no hysteresis effects are observed at $B^\star$. Although crystal-field effects are expected to be negligible in the Hund's rule ground-state multiplet of the Gd^{3+} ion, a magnetic anisotropy is clearly observed in these compounds.

To understand the observed magnetic structure and reproduce the magnetostriction and magnetic susceptibility data, we find it necessary to consider the spin-spin exchange interactions and their dependence on the lattice distortions, the dipolar interactions, and the crystal-field effects due to the mixing of the terms ^8S and ^6P as a consequence of the spin-orbit coupling.

The exchange couplings and their dependence on lattice distortions were estimated from first-principles DFT based calculations, while the crystal-field model and parameters were obtained from second-order perturbation theory. The final model parameters were obtained for each compound through a fitting procedure of the magnetostriction and magnetic susceptibility data. As a consistency check of the model parameters, we estimated the change in the Néel temperature with an applied hydrostatic pressure which shows and excellent agreement with the expected value from Ehrenfest's thermodynamic equations (see Appendix D).

Our model can fully account for the observed experimental data in $GdCoIn_5$ and $GdRh(In_{1-x}Cd_x)_5$ ($x = 0$ and 0.025), including the observed spin-flop transition and the absence of evidence of tetragonal symmetry breaking in these compounds. The main assumption is that the magnetically ordered state is a spatially inhomogeneous mixture of the two possible degenerate ground states. This assumption is needed to explain the absence of asymmetry, in the magnetic susceptibility and magnetostriction, between the $\hat{a}$-axis and the $\hat{b}$-axis measurements. Further experiments are needed to verify the mixed states hypothesis in these compounds. For instance, it would be interesting to measure the dependence of the spin polarization with the applied magnetic field.

Interestingly, there are other examples in the literature of tetragonal Gd-based compounds that show a similar behavior, i.e., antiferromagnetic order with magnetic anisotropy below T_N and a sudden change of the forced magnetostriction under a moderate magnetic field: $GdNi_2B_2C$ (Refs. [5,15]), $GdAg_2$ (Ref. [36]), and $GdRu_2Si_2$ (Ref. [37]) among others. The model discussed here could apply also to these cases.

ACKNOWLEDGMENTS

We are supported by PIPs 112-201101-00832, 112-201501-00506, and 2015-0364 GI of CONICET, SECTYP-UNCU 06/C489 of Universidad Nacional de Cuyo and PICTs 2013-1045, 2016-0204, and 2015 0869 of the ANPCyT. R.L.S. acknowledges FAPEMIG-MG (APQ-02256-12) and CAPES Foundation (Brazil) for grant EST-SENIOR-88881.119768/2016-01.

APPENDIX A: SIMPLIFIED MODEL

In this Appendix, we solve, at the mean-field level, a simplified model that captures the main magnetoelastic properties of the system in the ordered phase. We focus the analysis on the modifications of the lattice parameters in the a-b plane, which present sudden changes when a strong enough longitudinal magnetic field is applied. In the absence of an external magnetic field and assuming a C-AFM correlated state, the model reads

$$\mathcal{F} = \gamma_1 S_c^2 + \gamma_2(\delta a - \delta b)\left(S_a^2 - S_b^2\right) \tag{A1}$$

$$+ \beta_1(\delta a - \delta b) + \beta_2(\delta a + \delta b) \tag{A2}$$

$$+ \frac{C}{2}(\delta a^2 + \delta b^2) - \lambda\left(S_a^2 + S_b^2 + S_c^2 - 1\right). \tag{A3}$$

Here, the first two terms stem from the crystal field and the dipolar interaction. The third and fourth terms are due to the dependence of the exchange interactions on the lattice parameters. The fifth term is the elastic energy and in the last term, λ is a Lagrange multiplier included to enforce the spin normalization $|\vec{S}|^2 = 1$. The parameters of the model are given by

$$\gamma_1 = \left(\frac{\delta E_D}{S^2} + B_2\right) > 0, \tag{A4}$$

where $\delta E_D = E_D(\text{C-AFM}_{ac}) - E_D(\text{C-AFM}_{aa}) \sim 0.74$ K, is the difference in dipolar energy between the C-AFM$_{ac}$ and C-AFM$_{aa}$ phases. $\gamma_2 = A$ is given by the variation of the crystal field with lattice distortions [see Eq. (4)]. $\beta_1 = (\frac{dJ_0^a}{da} + \frac{dJ_0^a}{db})S^2$ and $\beta_2 = \frac{dJ_1}{da}S^2$ are given by the variation of the nearest neighbor and in-plane diagonal magnetic couplings with the lattice distortions.

There are four sets of distortions and spin projections that satisfy $\partial\mathcal{F}/\partial\ell = 0$ for all $\ell \in \{\delta a, \delta b, S_a, S_b, S_c, \lambda\}$:

Magnetic order	S_a	S_b	S_c	δa	δb	Energy
C-AFM$_{aa}$	1	0	0	$-\frac{1}{C}(\gamma_2+\beta_1+\beta_2)$	$\frac{1}{C}(\gamma_2+\beta_1-\beta_2)$	$-\frac{1}{2C}[(\gamma_2+\beta_1)^2+\beta_2^2]$
C-AFM$_{bb}$	0	1	0	$\frac{1}{C}(\gamma_2+\beta_1-\beta_2)$	$-\frac{1}{C}(\gamma_2+\beta_1+\beta_2)$	$-\frac{1}{2C}[(\gamma_2+\beta_1)^2+\beta_2^2]$
C-AFM$_{ac}$	0	0	1	$-\frac{1}{C}(\beta_1+\beta_2)$	$\frac{1}{C}(\beta_1-\beta_2)$	$\gamma_1-\frac{1}{2C}[\beta_1^2+\beta_2^2]$
C-AFM$_{bc}$	0	0	1	$\frac{1}{C}(\beta_1-\beta_2)$	$-\frac{1}{C}(\beta_1+\beta_2)$	$\gamma_1-\frac{1}{2C}[\beta_1^2+\beta_2^2]$

The ground state is doubly degenerate (C-AFM$_{aa}$ and C-AFM$_{bb}$) while C-AFM$_{ac}$ and C-AFM$_{bc}$ are degenerate higher energy states since $\gamma_1 > 0$ and $\gamma_2\beta_1 > 0$. C-AFM$_{ac}$ (C-AFM$_{bc}$) is however unstable with respect to a tilt of the spins, increasing S_a (S_b) . This fact preserves the spin-spin correlations (see Fig. 6 in the main text):

$$\left.\frac{d^2\mathcal{F}}{dS_a^2}\right|_{ac} = -\frac{4\beta_1\gamma_2}{C} - 2\gamma_1 < 0 \tag{A5}$$

A magnetic field along the $\hat{a}$ axis produces a magnetization $M\hat{a}$ in the states C-AFM$_{bb}$, C-AFM$_{ac}$ and C-AFM$_{bc}$ by tilting the spins along the same axis. This leads to a reduction of the energy of these states by $\sim B_a^2/T_N$ compared to the C-AFM$_{aa}$ state, which remains unchanged. At fields larger than

$$B^\star \sim \sqrt{T_N}\sqrt{\gamma_1 + \frac{1}{2C}\left[\gamma_2^2 + 2\gamma_2\beta_1\right]} \simeq \sqrt{T_N\gamma_1}, \tag{A6}$$

the energy of the C-AFM$_{ac}$ state becomes lower than the energy of the C-AFM$_{aa}$ state. Additionally the C-AFM$_{aa}$ state becomes unstable with respect to an increase in S_c:

$$\left.\frac{d^2\mathcal{F}}{dS_c^2}\right|_{ac} = \frac{4\beta_1\gamma_2}{C} + 2\gamma_1 - \frac{2B_a^2}{T_N} \sim 2\left[(B^\star)^2 - B_a^2\right]/T_N. \tag{A7}$$

This explains the transition between the metastable states C-AFM$_{aa}$ and C-AFM$_{ac}$ at $B = B^\star$.

APPENDIX B: THE GROUND STATE OF Gd^{3+}

According to the Hund rules, the state of maximum total angular momentum projection $M = 7/2$ of the ground-state multiplet $^8S_{7/2}$ is

$$|0, 7/2, 7/2, 7/2\rangle = \prod_{m=-3}^{3} f^\dagger_{m\uparrow}|0\rangle, \tag{B1}$$

where $f^\dagger_{l\sigma}$ creates a 4f electron with orbital angular momentum projection l and spin σ. The notation of the states is $|\mathcal{L}, \mathcal{S}, J, M\rangle$, where $\mathcal{L}$ ($\mathcal{S}$) is the total orbital angular momentum (spin), and J and M are the total angular momentum and its projection, respectively. The other states of the multiplet are obtained using repeatedly the lowering operator

$$\begin{aligned} J^- &= \mathcal{L}^- + \mathcal{S}^-, \\ \mathcal{L}^- &= \sum_\sigma \sum_{m=-2}^{3} a(m) f^\dagger_{m-1\sigma} f_{m\sigma}, \\ \mathcal{S}^- &= \sum_{m=-3}^{3} f^\dagger_{m\downarrow} f_{m\uparrow}, \\ a(m) &= \sqrt{12 - m(m-1)}. \end{aligned} \tag{B2}$$

The spin-orbit interaction

$$H_\lambda = \lambda \sum_i \mathcal{L}_i \cdot \mathcal{S}_i = \frac{\lambda}{2}\Bigg[\sum_{m=-2}^{3} a(m)(f^\dagger_{m\downarrow} f_{m-1\uparrow} + \text{H.c.}) + \sum_m m(f^\dagger_{m\uparrow} f_{m\uparrow} - f^\dagger_{m\downarrow} f_{m\downarrow})\Bigg] \tag{B3}$$

conserves the components of the total angular momentum J but modifies $\mathcal{L}$ and $\mathcal{S}$.

We obtain

$$\begin{aligned} H_\lambda|0, 7/2, 7/2, M\rangle &= V|1, 5/2, 7/2, M\rangle, \\ V &= \sqrt{14}\lambda. \end{aligned} \tag{B4}$$

The result is independent of M as can be easily shown using the fact that $\mathbf{J}$ commutes with H_λ. We obtain the ground-state multiplet $|g, M\rangle$ of Gd^{3+} solving a 2×2 matrix (the same for each M)

$$\begin{pmatrix} 0 & V \\ V & E \end{pmatrix}, \tag{B5}$$

where E is the energy difference between the multiplets $^6P_{7/2}$ and $^8S_{7/2}$ for $\lambda = 0$. Then, from the lowest lying state of Eq. (B5), we obtain with $u, v > 0$ and $u^2 = 1 - v^2$

$$\begin{aligned} |g, M\rangle &= u|0, 7/2, 7/2, M\rangle - v|1, 5/2, 7/2, M\rangle, \\ v^2 &= \frac{1}{2} - \frac{E}{4\sqrt{(E/2)^2 + V^2}}., \end{aligned} \tag{B6}$$

From optical experiments (Fig. 8 of Ref. [38]), we estimate $E \simeq 32\,000$ cm^{-1}. From the same reference, averaging the total spin-orbit splitting $\Delta = J_{\max}(J_{\max}+1)\lambda/(4S)$ between $J_{\max} = 6$ and $J_{\min} = 0$ for the ^7F terms ($\mathcal{L} = \mathcal{S} = 3$) of Eu^{3+} (configuration $4f^6$) and Tb^{3+} (configuration $4f^8$), we estimate $\Delta = 5500$ cm^{-1}, which implies $\lambda \simeq 1571$ cm$^{-1} \simeq 0.19$ eV. This gives $v^2 = 0.0307$. The value of λ is similar to $\lambda \simeq 1508$ cm^{-1} reported by Carnall *et al.* for Gd doped LaF_3 [39]. The effect of lattice distortions on the crystal-field is discussed on Ref [31].

APPENDIX C: ESTIMATION OF THE ELASTIC CONSTANTS

To obtain estimations for the elastic constants of $GdRhIn_5$ and $GdCoIn_5$, we used a combination of experimental results for related materials and density functional theory (DFT) calculations.

High-pressure x-ray diffraction (XRD) experiments on $CeRhIn_5$ and $CeCoIn_5$ report $K \sim 78$ GPa for the bulk modulus of both materials [28]. This leads to an elastic energy per

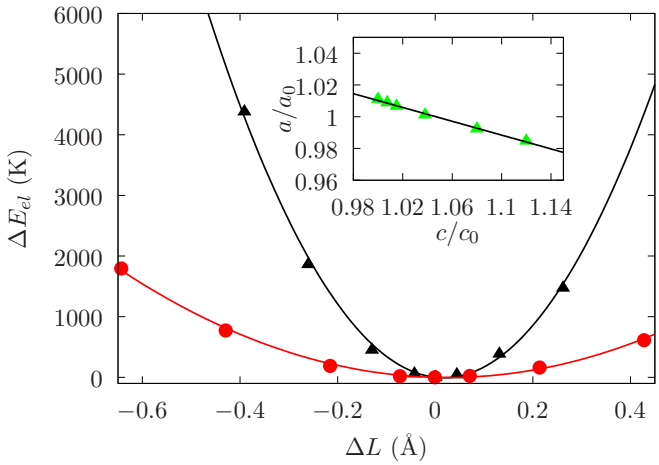

FIG. 7. Total energy vs $\delta a = \delta b = \Delta L$ for fixed $c = c_0$ (black triangles) and vs $\delta c = \Delta L$ for fixed $a = b = a_0$ (red disks). The lines are quadratic fits. (Inset) Deformation on a lattice parameter due to a change on c, relative to the equilibrium values a_0 and c_0, respectively. The line is a linear fit used to extract the Poisson's ratio.

atom

$$E_{el}(\delta a, \delta b, \delta c) = \frac{1}{2}E\left(c\,\delta a^2 + c\,\delta b^2 + \frac{a^2}{c}\,\delta c^2\right).$$

Here, $E = 3K(1-2\nu)$ is the Young modulus assuming an isotropic material where ν is Poisson's ratio. This results in anisotropic elastic constants along the $\hat{a}$-$\hat{b}$ and $\hat{c}$ axes, $C_{el}^{ab} = Ec$ and $C_{el}^{c} = Ea^2/c$, respectively. Using $\nu \sim 0.22$ (see below), we obtain $C_{el}^{a} \sim 71\,000$ K/Å^2 and $C_{el}^{c} \sim 27\,000$ K/Å^2.

The DFT calculations were performed using a supercell of $2 \times 2 \times 2$ unit cells. In Fig. 7, we show the change on the total energy as one of the unit cell lattice parameters (a or c) is changed. The quadratic behavior allows us to obtain the young modulus in both situations resulting

$$C_{el}^{a} = 52\,000\text{K/Å}^2 \text{ and } C_{el}^{c} = 8000\text{K/Å}^2.$$

We have also computed the Poisson's ratio [see Fig. 7(b)] resulting in $\nu \sim 0.22$.

APPENDIX D: PREDICTED EFFECT OF PRESSURE ON T_N

As a consistency check of the model parameters we calculate here the change of T_N with external pressure. We find a good agreement between the model results and the inferred from Ehrenfest's thermodynamic equations (approximately 0.8 and 1.2 K/GPa, respectively, see below).

An external hydrostatic pressure P produces changes $\delta b/b = \delta a/a = \delta c/c = -P/E$ on the lattice parameters. This modifies the Néel temperature for the C-AFM order

$$T_N = \frac{J(J+1)}{3k_B}(4\mathcal{J}_1 + 2\mathcal{J}_2 - 8\mathcal{J}_4), \tag{D1}$$

through the exchange coupling constants $\mathcal{J}_i$ dependence on the lattice parameters. For our model parameters (Table II), we find that the changes in T_N are dominated by the dependence of $\mathcal{J}_1$ on the lattice parameters

$$\delta T_N \sim -4P\frac{J(J+1)}{3k_B}\left(2a\frac{1}{E}\frac{d\mathcal{J}_1}{da} + c\frac{1}{E}\frac{d\mathcal{J}_1}{dc}\right). \tag{D2}$$

For an isotropic Young modulus of 131 GPa (see Appendix C), we obtain

$$\frac{\delta T_N}{P} \sim 0.8\text{K/GPa}. \tag{D3}$$

Ehrenfest's equations allow to relate the specific heat and the lattices changes on a second order transition

$$\frac{dT_N}{dP} = V_m T_N \frac{\Delta\alpha_V}{\Delta c_P}. \tag{D4}$$

For $GdCoIn_5$, using $V_m = 155.85$ Å^3, the lattice parameters of Table III, and the changes of specific heat and dilation reported in Ref. [7], we obtain

$$\Delta\alpha_V \sim 6 \times 10^{-6}\ \text{K}^{-1}, \quad \Delta c_P \sim 15\frac{\text{J}}{\text{mol K}}, \tag{D5}$$

which results in

$$\frac{\Delta T_N}{dP} \sim 1.2\text{K/GPa}. \tag{D6}$$

[1] A. Lindbaum and M. Rotter, in *Handbook of Magnetic Materials* (Elsevier B.V., Amsterdam, 2002), Vol. 14, pp. 307–362.

[2] M. Rotter, M. Loewenhaupt, M. Doerr, A. Lindbaum, H. Sassik, K. Ziebeck, and B. Beuneu, Phys. Rev. B **68**, 144418 (2003).

[3] S. Bacci, E. Gagliano, and E. Dagotto, Phys. Rev. B **44**, 285 (1991).

[4] O. P. Sushkov, J. Oitmaa, and Z. Weihong, Phys. Rev. B **63**, 104420 (2001).

[5] M. Rotter, A. Lindbaum, A. Barcza, M. El Massalami, M. Doerr, M. Loewenhaupt, H. Michor, and B. Beuneu, Europhys. Lett. **75**, 160 (2006).

[6] E. Granado, B. Uchoa, A. Malachias, R. Lora-Serrano, P. G. Pagliuso, and H. Westfahl Jr, Phys. Rev. B **74**, 214428 (2006).

[7] D. Betancourth, J. I. Facio, P. Pedrazzini, C. B. R. Jesus, P. G. Pagliuso, V. Vildosola, P. S. Cornaglia, D. J. García, and V. F. Correa, J. Magn. Magn. Mater. **374**, 744 (2015).

[8] P. G. Pagliuso, J. D. Thompson, M. F. Hundley, J. L. Sarrao, and Z. Fisk, Phys. Rev. B **63**, 054426 (2001).

[9] K. Łatka, R. Krniec, M. Rams, A. W. Pacyna, V. Zaremba, and R. Pöttgen, Z. Naturforsch., B: Chem. Sci. **59**, 947 (2004).

[10] M. Brooks and D. Goodings, J. Phys. C **1**, 1279 (1968).

[11] B. Bleaney, H. Scovil, and R. Trenam, Proc. R. Soc. Lond. A **223**, 15 (1954).

[12] K. Buschow, H. Algra, and R. Henskens, J. Appl. Phys. **51**, 561 (1980).

[13] D. Khomskii, *Transition Metal Compounds* (Cambridge University Press, Cambridge, 2014).

[14] J. I. Facio, D. Betancourth, P. Pedrazzini, V. F. Correa, V. Vildosola, D. J. García, and P. S. Cornaglia, Phys. Rev. B **91**, 014409 (2015).
[15] J. Jensen and M. Rotter, Phys. Rev. B **77**, 134408 (2008).
[16] P. S. Normile, M. Rotter, C. Detlefs, J. Jensen, P. C. Canfield, and J. A. Blanco, Phys. Rev. B **88**, 054413 (2013).
[17] Z. Fisk and J. Remeika, in *Handbook on the Physics and Chemistry of Rare Earths*, edited by K. Gshneidner and L. Eyring (North-Holland, Amsterdam, 1989), Vol. 12, p. 53.
[18] L. D. Pham, T. Park, S. Maquilon, J. D. Thompson, and Z. Fisk, Phys. Rev. Lett. **97**, 056404 (2006).
[19] G. Schmiedeshoff, A. Lounsbury, D. Luna, S. Tracy, A. Schramm, S. Tozer, V. Correa, S. Hannahs, T. Murphy, E. Palm *et al.*, Rev. Sci. Instrum. **77**, 123907 (2006).
[20] E. Göran, *Handbook of Giant Magnetostrictive Materials* (Academic Press, San Diego, CA, 2000).
[21] E. Stryjewski and N. Giordano, Adv. Phys. **26**, 487 (1977).
[22] D. C. Johnston, Phys. Rev. B **96**, 224428 (2017).
[23] D. Betancourth, V. F. Correa, and D. J. García, J. Low Temp. Phys. **179**, 90 (2015).
[24] N. Van Hieu, T. Takeuchi, H. Shishido, C. Tonohiro, T. Yamada, H. Nakashima, K. Sugiyama, R. Settai, T. D. Matsuda, Y. Haga *et al.*, J. Phys. Soc. Jpn. **76**, 064702 (2007).
[25] E. Callen and H. B. Callen, Phys. Rev. **139**, A455 (1965).
[26] R. Amaral, R. Lora-Serrano, D. J. García, W. Iwamoto, D. Betancourth, J. Cadogan, S. Muñoz-Pérez, M. Avdeev, R. Cobas-Acosta, E. Bittar *et al.*, Intermetallics **98**, 161 (2018).
[27] A. F. García-Flores, J. S. Matias, D. J. Garcia, E. D. Martínez, P. S. Cornaglia, G. G. Lesseux, R. A. Ribeiro, R. R. Urbano, and C. Rettori, Phys. Rev. B **96**, 165430 (2017).
[28] R. S. Kumar, A. L. Cornelius, and J. L. Sarrao, Phys. Rev. B **70**, 214526 (2004).
[29] R. S. Kumar, H. Kohlmann, B. E. Light, A. L. Cornelius, V. Raghavan, T. W. Darling, and J. L. Sarrao, Phys. Rev. B **69**, 014515 (2004).
[30] N. Shannon, B. Schmidt, K. Penc, and P. Thalmeier, Eur. Phys. J. B **38**, 599 (2004).
[31] See Supplemental Material at http://link.aps.org/supplemental/10.1103/PhysRevB.99.134406 for an estimation of the change of the crystal field and the evolution of the exchange couplings under lattice deformations.
[32] Y. Zhu, M. Suenaga, and A. Moodenbaugh, Philos. Mag. Lett. **62**, 51 (1990).
[33] S. Semenovskaya and A. G. Khachaturyan, Phys. Rev. Lett. **67**, 2223 (1991).
[34] Y. Shapira and S. Foner, Phys. Rev. B **1**, 3083 (1970).
[35] R. W. Wang and D. L. Mills, Phys. Rev. B **50**, 3931 (1994).
[36] N. Mehboob, M. Rotter, M. Doerr, E. Royanian, H. Müller, A. Grytsiv, and Y. Skourski, Solid State Commun. **151**, 1112 (2011).
[37] A. Devishvili, Ph.D. thesis, Universität Wien, 2010.
[38] G. H. Dieke and H. Crosswhite, Appl. Opt. **2**, 675 (1963).
[39] W. Carnall, G. Goodman, K. Rajnak, and R. Rana, J. Chem. Phys. **90**, 3443 (1989).